46th AIAA Aerospace Sciences Meeting and Exhibit
7 - 10 January 2008, Reno, Nevada

AIAA 2008-954

Mixture Fraction Measurement in the Flowfield from a Coaxial Injector

A. Abdelhafez* **and A. K. Gupta†**
Department of Mechanical Engineering, University of Maryland
College Park, MD 20742

Knowledge of the spatial distribution of mixture fraction is very important for assuring safe and reliable operation of almost all combustion systems. A diagnostic technique, based on the principles of absorption spectroscopy, is being developed to provide insightful information on the variation of local mixture fractions inside the unconfined flowfield of a shear coaxial injector. Single-phase non-reacting gaseous-flow conditions are considered. Methane is injected as a trace gas into one of the two streams upstream of the injector. The flowfield is illuminated at the location of measurement by a collimated beam of infrared laser radiation at the 1.66-μm peak wavelength of the first vibrational absorption band of methane in the IR region. Based on the measured transmitted (i.e. non-absorbed) radiation, the line-of-sight value of local methane concentration is determined according to the Beer-Lambert law of gas absorbitivity. Abel inversion is performed to deconvolute the line-of-sight values to a 2-D distribution within a centerline plane of the flowfield, under the assumption of axisymmetric flow. The 2-D profile of methane concentration is used to calculate the mixture fraction distributions of central and annular gases of the injector. A sensitivity of 50 ppm·m (concentration-pathlength product) has been achieved with 95% accuracy over a signal-averaging time of two seconds. The system has been tested at different velocity and density ratios of the injector jets. It was found that a velocity or density ratio of unity results in poorest mixing, i.e., values of velocity and density ratios far from unity yield in enhanced mixing. The distribution of mixture fraction is more sensitive to changes in velocity ratio than to changes in density ratio. The results obtained here on mixing under single-phase non-reacting conditions prove the system feasibility in providing a powerful diagnostic technique for mixture fraction measurements.

I. Introduction

Optical sensors, based on semiconductor lasers, are at the threshold of routine applications in gas analysis. These sensors are used increasingly for industrial and environmental monitoring applications, whenever sensitive, selective, and fast in-situ analysis in the near- and mid-infrared spectral region is required. Semiconductor diode lasers are attractive sources for practical applications, due to their compactness, low cost, robustness, and relative ease of use. Diode-laser-based absorption-spectroscopy techniques with commercially available room-temperature light sources have been applied to probe transitions of vibrational overtone and combination bands of various species in the near-IR region, including H_2O (1.34 – 1.39 μm), N_2O (1.52 μm), CO (1.56 μm), CO_2 (1.57 μm), CH_4 (1.65 μm), and NO (1.8 μm).[1–8] The detection sensitivity, however, is limited by the relatively weak line strengths associated with these bands. Recent developments in semiconductor diode-laser technology, based on strained InGaAs/InP materials, have extended the range of available laser wavelengths to 2.0 μm, allowing access to stronger vibrational overtones of important combustion species, including CO_2 and H_2O.[9,10]

Coincidences of molecular-absorption lines and diode lasers emission spectra are expected to be abundant, because diode lasers are tunable and available in the wide infrared regions, where the vibrational absorption bands of many molecules lie. Therefore, a sensor system can be applied to various gases just by replacing the laser. Moreover, the compactness and mechanical stability of diode lasers are favorable for the portability of sensors. Few studies have shown the usefulness of tunable diode lasers for sensitive detection of trace gases, especially methane.[11-17] Cassidy estimated that 5 ppm of methane in a 1-m optical path length would be detectable by second-harmonic detection, if a diode laser operating at 1.65 μm were available.[13] Reid et al. demonstrated that 1 ppb of methane at atmospheric pressure could be detected in a 32-m path length by scanning a liquid-He-cooled Pb-salt laser across methane-absorption lines near 7.4 μm.[15] Koga et al. performed an open-air methane monitoring, using a PbSnTe laser with a microcomputer for signal processing and attained a sensitivity of 3 ppm for a 10-ms measurement time.[16] However, when room-temperature operation is mandatory, the wavelength of semiconductor laser sources is limited to the region below 2 μm, where methane absorption is weak. Chan et al. reported on a long-distance methane-sensing system that uses a 1.3- or a 1.6-μm light-emitting diode in combination with optical fibers.[17] Mohebati and King investigated the differential-absorption detection of methane by a 1.33-μm InGaAsP multimode diode laser and optical fibers.[18] Sensitivities of 1000-2000 ppm for a 1-m optical path length were obtained by these room-temperature systems.[17,18] In another investigation, methods for real-time remote sensing of

* Graduate Student, Student Member AIAA
† Professor, Fellow AIAA, email: akgupta@umd.edu

methane were demonstrated, which use a 1.66-μm InGaAsP distributed-feedback (DFB) laser.[19] A high sensitivity of 0.3 ppm·m (concentration-pathlength product) was achieved for a signal-averaging time of 1.3 s.

To achieve high detection sensitivity, it is desirable to use as strong an absorption line as possible. Methane has strong vibrational bands at 2.3 and 3.3 μm, see Figure 1. At present, however, it is difficult to make diode lasers of wavelengths longer than 2 μm that operate at room temperature. The strongest band of methane in the region below 2 μm has a center located at 1.665 μm. This present work utilizes the principles of absorption spectroscopy for in-situ non-intrusive determination of mixture fractions in the flowfield from a shear coaxial gas/gas injector using methane as a trace gas at the 1.66-μm band. The variations of mixture fractions are quantified at different conditions of velocity and density ratios. The goal is to reduce the minimum detectable methane concentration needed for the quantification of variations in mixture fractions. Efforts should also be made to extend the system applicability to the cryogenic two-phase flows of rocket-engine injectors.

II. Experimental Setup and Test Matrix

An absorption-detection diagnostic technique is being developed to provide insightful information on the variation of local mixture fractions inside the unconfined flowfield of a shear coaxial injector. Single-phase non-reacting gaseous-flow conditions are considered. The principles of absorption spectroscopy are implemented for mixture fraction measurements by injecting a trace gas (methane) into one of the two streams upstream of the injector. The concentration of methane is measured non-intrusively at the desired location of the flowfield by emitting infrared radiation at the 1.66-μm peak wavelength of the first vibrational absorption band of methane in the IR region, see Figure 1. A laser diode (LD) of 7 mW optical power is used. Optical lenses collimate the emitted laser beam for local line-of-sight measurements. A photodetector (PD) measures the intensity of the transmitted (i.e. non-absorbed) radiation, thus giving an indication of the amount absorbed, which is calibrated for the value of local methane concentration according to the Beer-Lambert law of gas absorbitivity

$$A = \ln\left(\frac{I_o - I_b}{I_T - I_b}\right) = \varepsilon\, b\, c \qquad (1)$$

where: $A \equiv$ absorbance
$I_o \equiv$ reference (laser-diode) intensity
$I_b \equiv$ background noise
$I_T \equiv$ transmitted (detected) intensity
$\varepsilon \equiv$ molar absorbitivity of methane (5×10^4 cm^2/mol at 1 atm and 300 K)
$b \equiv$ path length [cm]
$c \equiv$ local methane concentration [mol/cm^3]

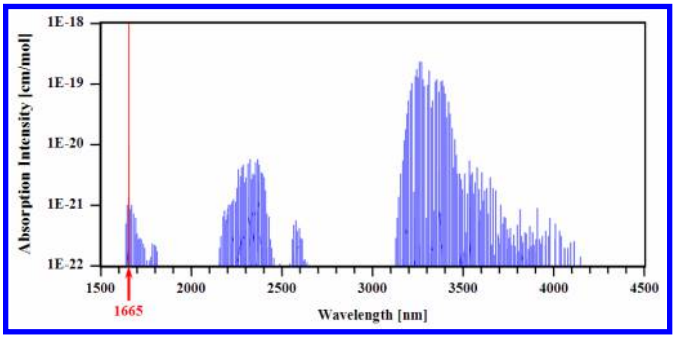

Figure 1. Vibrational bands of methane in IR region

Since the obtained methane concentrations are line-of-sight values, Abel inversion is performed to deconvolute the data and get a planar 2-D profile of the concentration distribution within a centerline plane of the flowfield. The numerical algorithms described in Ref. [20] and [21] are used, assuming axisymmetric flow. The 2-D profile of methane concentration is then converted to the corresponding mixture fraction distribution using ideal-gas relations. Knowing the reference methane mixture fraction upstream of the injector, the distribution of methane mixture fraction within the flowfield centerline plane can be used to calculate and plot the variations in mixture fractions of both central and annular injector flows within the centerline plane.

Thermal flow meters/controllers of 0.2% full-scale accuracy are used to control the flow rates of both central and annular flows, as well as methane. An optical bandwidth filter (1.66 μm, 12 nm FWHM) before the PD minimizes the effect of background noise, thus increasing the detection accuracy and sensitivity. A schematic of the experimental setup is shown in Figure 2. A data-logger with internal amplification and analog-to-digital conversion acquires the PD output at a rate of 200 Hz over a signal-averaging time of two seconds with a sensitivity of 1 μV. This acquisition process is repeated 15 times at each location of the flowfield, in order to average out any fluctuations due to turbulence. Significant statistical information is thus obtained locally on the mean and standard deviation of methane concentration, and globally on the system sensitivity and accuracy. The whole detection system is movable along a 3-D traverse mechanism to scan the entire flowfield.

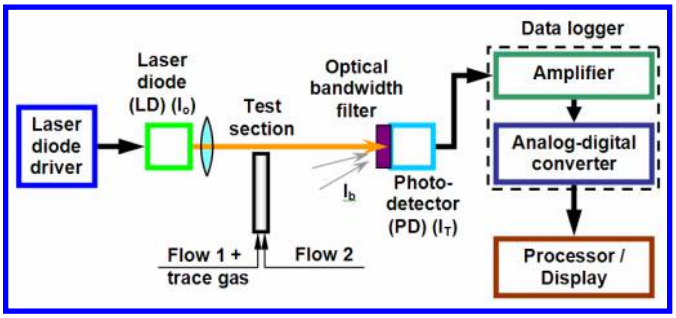

Figure 2. Schematic of the experimental setup

The test section of the experimental setup comprises a shear coaxial injector that consists of two coaxial tubes. The outer tube has dimensions of 0.5 in OD and 0.425 in ID, whereas the dimensions of the inner one are 0.375 in OD and 0.3 in ID. Therefore, the hydraulic diameters of both annular and central flows are 0.05 in and 0.3 in, respectively. Table 1 lists the test matrix for the results presented here. Although the test rig allows for methane injection in either the central or annular flows of the injector, methane was injected in the central flow for all the results presented here, in order to facilitate easy determination of the system sensitivity, as described in the next section. The reference methane concentration in the central flow upstream of the injector was kept fixed to a value of 10,000 ppm (1%) for all cases listed in Table 1.

Cases 1 – 5 in Table 1 highlight the effect of velocity ratio at a density ratio of unity. Air was used as both central and annular flows, in order to achieve this density ratio. Cases 6 – 11, on the other hand, quantify the effect of density ratio at a velocity ratio of unity. Whereas air was used again as an annular flow, a mixture of helium and argon formed the central flow of the injector. Different mixture compositions yielded different central-flow densities, in order to examine the effect of central-to-annular density ratio. Meanwhile, the mass flow rate of the He-Ar mixture was adjusted from one case to another to maintain an injector velocity ratio of unity. It is to be noted that He-Ar mixtures have a wide density span from 0.162 kg/m^3 for pure helium to 1.62 kg/m^3 for pure argon (i.e., an order of magnitude higher).

Table 1. Test Matrix

Methane injected in central flow
Reference methane concentration = 10,000 ppm (1%)

Case No.	$\dot{m}_i$ [g/s]	$\dot{m}_o$ [g/s]	$\frac{v_i}{v_o}$	$\frac{\rho_i}{\rho_o}$	$\frac{(\dot{m}v)_i}{(\dot{m}v)_o}$
Effect of Velocity Ratio Central flow = Air. Annular flow = Air					
1	2.683	2.385	0.50	1	0.563
2	2.683	1.590	0.75	1	1.266
3	2.683	1.193	1.00	1	2.250
4	2.683	0.954	1.25	1	3.516
5	2.683	0.795	1.50	1	5.063
Effect of Density Ratio Central flow = Mixture of He and Ar. Annular flow = Air					
6	0.741	2.385	1	0.138	0.311
7	3.220	2.385	1	0.600	1.350
8	4.293	2.385	1	0.800	1.800
9	5.367	2.385	1	1.000	2.250
10	6.440	2.385	1	1.200	2.700
11	7.410	2.385	1	1.381	3.107

Some key points are to be noted here:

- Both velocity and density ratios have a value of unity for cases 3 and 9
- Cases 4 and 5 have velocity ratios greater than one, which simulates an inverse burner
- Cases 6 – 8 simulate burners utilizing low-density fuels, such as hydrogen and natural gas, as well as moderate density fuels, such as acetylene.
- Case 9 simulates burners utilizing fuels, such as ethylene and ethane, with densities very close to that of air
- Cases 10 and 11 simulate burners utilizing high-density fuels, such as LPG

III. Results and Discussion

System Sensitivity

The system sensitivity was determined by comparing the reference methane concentration upstream of the injector to its value at the injector exit with a line-of-sight passing through the injector centerline. In cylindrical coordinates, this point corresponds to the origin (r = 0, z = 0) of the coordinate system. The reason residing behind the choice of this point is that it lies at the center of the potential core of central flow, where no mixing has taken place between the central and annular flows yet. Thus, the concentration of methane at the origin should almost be equal to its reference value upstream of the injector, up to the sensitivity limit. The reference value was lowered gradually, until the error between the origin and reference values reached 5% (arbitrarily chosen here). At this instant, the reference value was about 6500 ppm, which dictates the detection limit of the system. Since the pathlength at the flowfield origin is 0.3 in (0.762 cm), the 6500-ppm detection limit corresponds to a system sensitivity of 50 ppm·m.

Figure 3 illustrates the above procedure of determining the system detection limit. Plotted is the methane concentration at the flowfield origin versus the reference concentration upstream of the injector. Shown are two scenarios; one is for the case of a perfect system (black 45° line), and the other is for the actual system indicated by the blue dots that turn red after the detection limit is breached. The two indicated error values indicate that the detection limit is just below 6500 ppm for an acceptable accuracy of 95%.

It is worth noting here that the reference methane concentration upstream of the injector was lowered to the detection limit, and beyond, in order to determine the system sensitivity. The system cannot be operated at its detection limit while quantifying the effects of velocity and density ratios of central and annular flows. Methane concentration has its peak flowfield value at the origin, and this concentration decreases along both radial and axial directions. Therefore, if the system were to be operated at its detection limit while quantifying the effects of velocity and

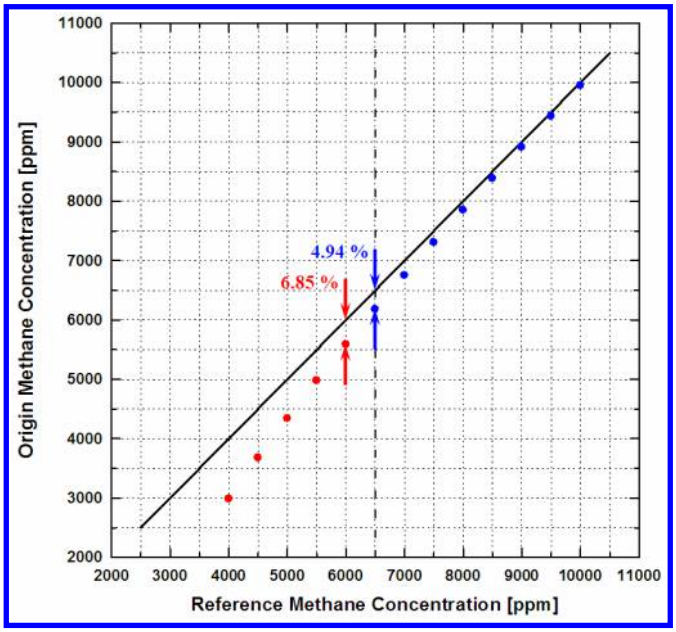

Figure 3. Comparison of methane concentration at flowfield origin to reference methane concentration upstream of injector. Black 45° line represents perfect system. Blue: actual system (accuracy > 95%). Red: actual system (accuracy < 95%). Two error values indicated; blue: acceptable, red: unacceptable. Detection limit ≈ 6500 ppm.

density ratios, methane concentrations all over the flowfield will be below the limit, and thus of unacceptable accuracy. For this reason, the following analyses of the effects of velocity and density ratios were conducted at a reference methane concentration of 10,000 ppm (1%).

Effect of Jet Velocity Ratio

The effect of injector central-to-annular velocity ratio is highlighted through a comparison of cases 1 – 5 given in Table 1. Figure 4 shows the mixture fraction profiles of central flow for these five cases within 6.5 jet-diameters downstream of the injector exit. All mixture fractions below 0.65 are not indicated (black region), as they correspond to measured methane concentrations below the system detection limit and thus of unacceptable accuracy. Therefore, the color scale represents central-flow mixture fractions of 0.65 – 1.0 only.

Three main observations can be made from Figure 4. First, for central-to-annular velocity ratios less than unity, increasing the velocity ratio results in poorer mixing. Second, this trend is reversed for ratios greater than unity. Third, case 3, with a ratio of 1.0, shows a spike in central-jet potential core length. These observations are concurred by Figure 5, where the variation of central-jet potential core length is plotted with injector central-to-annular velocity ratio. The potential core length is based on a centerline central-flow mixture fraction of 0.9 (arbitrarily chosen) and was chosen as a good representative of mixing quality.

Such behavior can be explained by understanding the mixing mechanism in flowfields of shear coaxial injectors. This is achieved by monitoring the velocity potential driving the shear layer between central and annular jets. For velocity ratios other than unity, a velocity gradient exists across the shear layer. This gradient peaks at the injector exit (where the central and annular jets first meet) and generates small-scale Kelvin-Helmholtz vortical instabilities within the shear layer. These instabilities agglomerate and grow in size, as the jets propagate downstream, which results in increasing

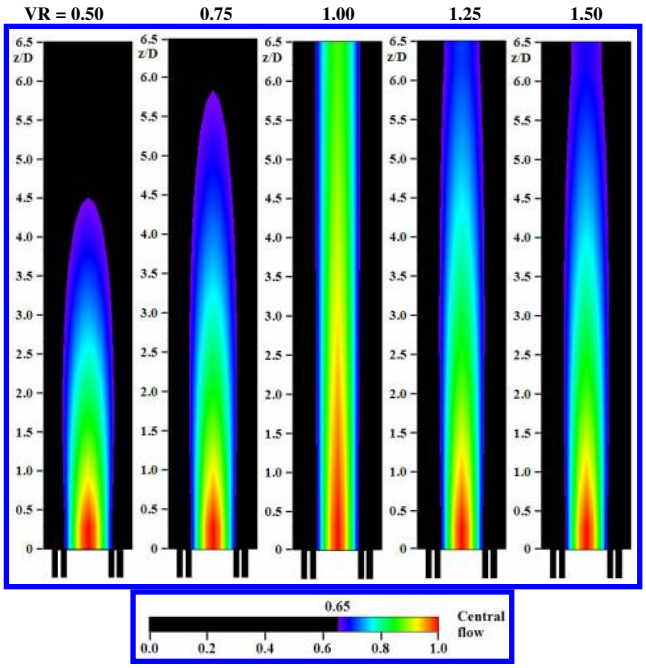

Figure 4. Central-flow mixture fraction profiles for cases 1 – 5 (left to right) within 6.5 jet-diameters downstream of the injector exit. Black: mixture fractions < 0.65. Color: mixture fractions of 0.65 – 1.0.

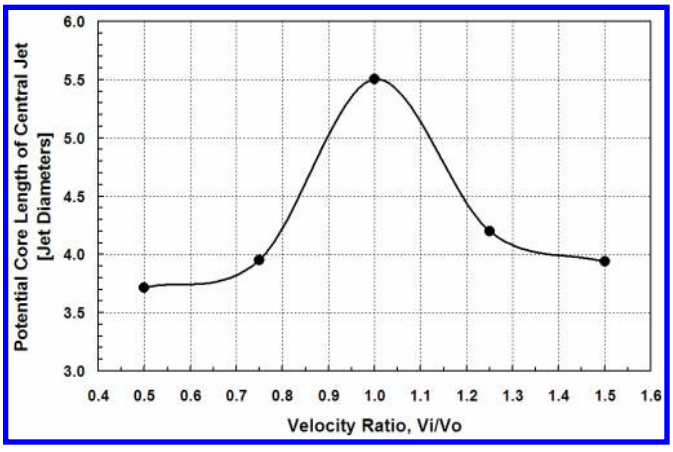

Figure 5. Variation of central-jet potential core length with injector central-to-annular velocity ratio. Potential core length based on a centerline central-flow mixture fraction of 0.9 (arbitrarily chosen).

shear layer thickness. The vortices within the shear layer consume the potential cores of both central and annular jets by stirring and mixing them up. Therefore, as the shear-layer velocity potential is increased from cases 3 to 2 and 4 to 5, a better mixing quality can be obtained.

Case 3 is a clear example of poorest mixing quality, due to the lack of any velocity potential at the interface of central and annular jets. No shear layer exists between them; thus, the potential cores propagate considerably downstream, before any significant mixing takes place. However, the potential cores do not propagate indefinitely—eventual mixing must occur. This is attributed to the existence of a shear layer between the annular jet and the stagnant surroundings adjacent to the flowfield. This shear layer has a velocity potential of its own, which induces vortices that grow steadily to consume the annular potential core first, before interacting with the central one. For this reason, case 3 is observed to have the longest central-jet potential core, as compared to the other cases shown in Figure 4.

An additional observation to be made from Figures 4 and 5 is that cases 4 and 5, which simulate an inverse burner, have longer central-jet potential cores, as compared to cases 1 and 2. This does not necessarily mean poorer mixing. As Table 1 shows, the mass flow rate of annular flow decreases from cases 1 to 5, which implicitly means higher flowfield mixture fractions of central flow. Nevertheless, the effect of increasing the central-to-annular velocity ratio from cases 4 to 5 still overcomes the effect of decreasing the mass flow rate of annular flow, and the central-jet potential core length decreases from cases 4 to 5.

Effect of Jet Density Ratio

Changing the central-to-annular jet density ratio of the injector was found to yield a behavior, which is qualitatively similar to that of the velocity ratio. This finding is obtained from Figures 6 and 7. Cases 6 – 11 are compared to each other in Figure 6 based on their central-flow mixture fraction profiles within 6.5 jet-diameters downstream of the injector exit. Figure 7, on the other hand, shows the variation of central-jet potential core length plotted with injector central-to-annular density ratio. It can be seen from both figures that for density ratios less than unity, decreasing the density ratio results in better mixing and shorter central-jet potential cores, as was observed earlier in the analysis of velocity-ratio effect. Moreover, the opposite is true for density ratios greater than unity, i.e., mixing is enhanced as the density ratio is increased. Furthermore, a spike in central-jet potential core occurs in case 9, with a density ratio of 1.0.

These observations of the effect of density ratio can be explained in the same manner as the effect of velocity ratio. Kelvin-Helmholtz instabilities can be induced by the existence of a density gradient across the interface of central and annular flows, similar to the effect of a velocity gradient.

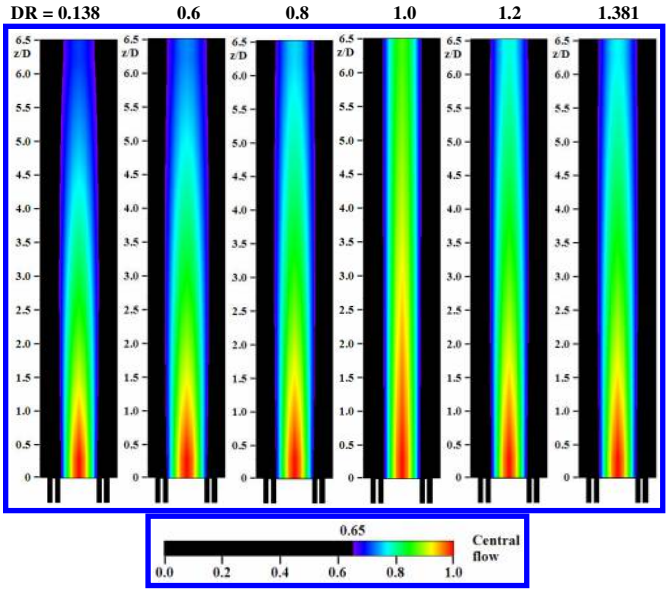

Figure 6. Central-flow mixture fraction profiles for cases 6 – 11 (left to right) within 6.5 jet-diameters downstream of the injector exit. Black: mixture fractions < 0.65. Color: mixture fractions of 0.65 – 1.0.

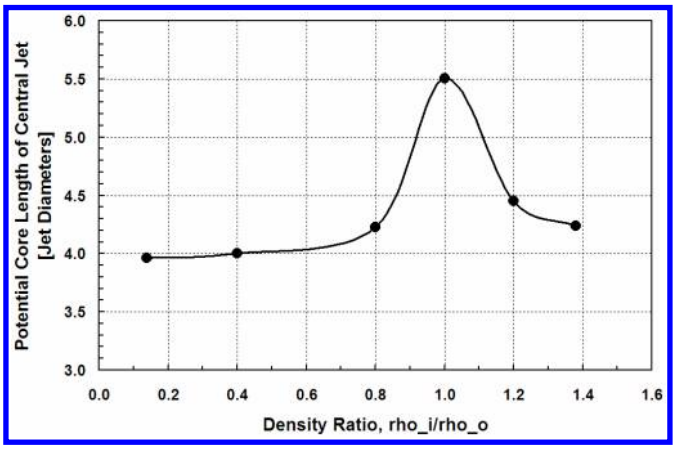

Figure 7. Variation of central-jet potential core length with injector central-to-annular density ratio. Potential core length based on a centerline central-flow mixture fraction of 0.9 (arbitrarily chosen).

The density difference across this interface renders it unstable and susceptible to triggering of instabilities, which curve and stretch it. As soon as these instabilities initiate close to the injector exit, they tend to magnify and agglomerate, allowing for island formation and resulting in gradual growth of the interface thickness. Consequently, mixing takes place gradually, accompanied by the consumption of the central and annular potential cores. It should be noted that a velocity potential is more effective in inducing Kelvin-Helmholtz instabilities than a density gradient, which explains the poorer mixing and overall higher values of central-jet potential core length

accompanying cases 6 – 11 of the density-ratio effect, compared to cases 1 – 5 of the velocity ratio. For the very same reason, it can be observed that a reduction in potential core length by 0.5 jet diameters is achieved by decreasing the density ratio all the way from 0.8 down to 0.14, whereas the same reduction in core length can be achieved just by changing the velocity ratio from 0.75 to 0.5.

In the absence of both the density and velocity gradients, case 9, the curve of central-jet potential core length spikes, which is similar to the behavior of case 3 (described earlier). No shear layer and hardly any perturbations exist at the interface of central and annular flows to induce any vortices or instabilities close to the injector exit. However, mixing does take place gradually further downstream, due to vortices that generate within the shear layer between annular flow and stagnant surroundings. Those vortices grow in size to consume the potential core of annular flow first, before they interact with the central flow. This results in a longer central-jet potential core under these conditions.

IV. Conclusions

A diagnostic technique, based on the principles of absorption spectroscopy, is being developed and used to provide insightful information on the variation of local mixture fractions inside the unconfined flowfield from a shear coaxial injector. Under single-phase non-reacting gaseous-flow conditions, a sensitivity of 50 ppm·m (concentration-pathlength product) has been achieved with 95% accuracy over a signal-averaging time of two seconds, using methane as the trace gas. When testing the system at different velocity and density ratios of the injector jets, it was found that a velocity or density ratio of unity results in poor mixing, i.e., values of velocity and density ratios far from unity result in enhanced mixing. The distribution of mixture fraction is more sensitive to changes in velocity ratio than it is to changes in density ratio.

Acknowledgments

This work was supported by the Space Vehicle Technology Institute under grant NCC3-989 jointly funded by NASA and DoD within the NASA Constellation University Institutes Project, with Claudia Meyer as the Project Manager. The DoD work was supported by the USAF. This support is gratefully acknowledged.

The help provided by Adam Kareem in data acquisition and analysis is gratefully acknowledged.

References

[1]Baer, D. S., Nagali, V., Furlong, E. R., Hanson, R. K., and Newfield, M. E., "Scanned- and fixed-wavelength absorption diagnostics for combustion measurements using a multiplexed diode-laser sensor system," AIAA Journal, Vol. 34, 1996, pp. 489–493.

[2]Sonnenfroh, D. M. and Allen, M. G., "Absorption measurements of the second overtone band of NO in ambient and combustion gases with a 1.8-μm room-temperature diode laser," Applied Optics, Vol. 36, 1997, pp. 7970–7977.

[3]Nagali, V., Furlong, E. R., Chou, S. I., Mihalcea, R. M., Baer, D. S., and Hanson, R. K., "Diode-laser sensor system for multi-species and multi-parameter measurements in combustion flows," 31st Joint Propulsion Conference, San Diego, CA, 10–12 July 1995, AIAA 95-2684.

[4]Baer, D. S., Hanson, R. K., Newfield, M. E., and Gopaul, N. K., "Multiplexed diode-laser sensor system for simultaneous H_2O, O_2, and temperature measurements," Optics Letters, Vol. 19, Issue 22, 1994, pp. 1900–1902.

[5]Furlong, E. R., Baer, D. S., and Hanson, R. K., "Combustion control using a multiplexed diode laser sensor system," Twenty-Sixth Symposium (International) on Combustion, The Combustion Institute, Pittsburgh, PA, (1996), pp. 2851–2858.

[6]Nagali, V., Chou, S. I., Baer, D. S., and Hanson, R. K., "Tunable diode laser absorption measurements of CH_4 at elevated temperatures," Applied Optics, Vol. 35, 1996, pp. 4026–4032.

[7]Mihalcea, R. M., Baer, D. S., and Hanson, R. K., "Diode laser sensor for measurements of CO, CO_2, and CH_4 in combustion flows," Applied Optics, Vol. 36, 1997, pp. 8745–8752.

[8]Mihalcea, R. M., Baer, D. S., and Hanson, R. K., "A diode-laser sensor system for combustion emission measurements," Measurement Science and Technology, Vol. 9, 1998, 327–338.

[9]Mihalcea, R. M., Baer, D. S., and Hanson, R. K., "Diode-laser absorption measurements of CO_2 near 2.0 μm at elevated temperature," Applied Optics, Vol. 37, No. 36, 1998, pp. 8341–8347.

[10]Mihalcea, R. M., Baer, D. S., and Hanson, R. K., "Advanced Diode-Laser Absorption Sensor For In-Situ Combustion Measurements of CO_2, H_2O, and Gas Temperature," 36th Aerospace Sciences Meeting and Exhibit, Reno, NV, 12-15 Jan., 1998, AIAA-1998-237.

[11]Forrest, G. T., "Tunable diode laser measurement of methane, ethane, and water vapor in cigarette smoke," Applied Optics, Vol. 19, 1980, pp. 2094-2096.

[12]Cassidy, D. T. and Reid, J., "Atmospheric pressure monitoring of trace gases using tunable diode lasers," Applied Optics, Vol. 21, 1982, p. 1185.

[13]Cassidy, D. T., "Trace gas detection using 1.3-μm InGaAsP diode laser transmitter modules," Applied Optics, Vol. 27, 1988, pp. 610-614.

[14]Defreez, R. K. and Elliott, R. A., "External grating-tuned dual-diode-laser source for remote detection of coal gas methane," J. Opt. Soc. Am., Vol. 73, 1983, p. 1854.

[15]Reid, J., Sinclair, R. L., Grant, W. B., and Menzies, R. T., "High-sensitivity detection of trace gases at atmospheric pressure using tunable diode lasers," Optical and Quantum Electronics, Vol. 17, 1985, pp. 31-39.

[16]Koga, R., Kosaka, M., and Sano, H., "Field methane tracking with a portable and real-time open-gas monitor based on a CW-driven Pb-salt diode laser," Optics & Laser Technology, Vol. 17, June 1985, pp. 139-44.

[17]Chan, K., Ito, H., and Inaba, H., "10-km-long fiber-optic remote sensing of CH_4 gas by near infrared absorption," Applied Physics B: Lasers and Optics, Vol. 38, No. 1, 1985, pp. 11-15.

[18]Mohebati, A. and King, T. A., "Remote detection of gases by diode laser spectroscopy," Journal of Modern Optics, Vol. 35, 1988, pp. 319-324.

[19]Uehara, K. and Tai, H., "Remote detection of methane with a 1.66-μm diode laser," Applied Optics, Vol. 31, No. 6, 1992, pp. 809-814.

[20]Dasch, C. J., "One-dimensional tomography: a comparison of Abel, onion-peeling, and filtered backprojection methods," Applied Optics, Vol. 31, No. 8, March 1992, pp. 1146–1152.

[21]Gautam, V. and Gupta, A. K., "Spectroscopic Analysis of Fuel Lean Flames for Propulsion Applications," Proceedings of ASME Power Conference, Baltimore, MD, Mar 30 - Apr 1, 2004, PWR2004-52074.